IEEE Access
Multidisciplinary | Rapid Review | Open Access Journal

Received 4 June 2022, accepted 23 June 2022, date of publication 27 June 2022, date of current version 30 June 2022.

Digital Object Identifier 10.1109/ACCESS.2022.3186476

RESEARCH ARTICLE

Multifractal Analysis of Reservoir Rock Samples Using 3D X-Ray Micro Computed Tomography Images

MOHAMED SOUFIANE JOUINI[1], FATEH BOUCHAALA[2], MOHAMED KAMEL RIAHI[1], MOHAMED SASSI[3], HAMID ABDERRAHMANE[4], AND FAWAZ HJOUJ[1]

[1]Department of Mathematics, Khalifa University, Abu Dhabi, United Arab Emirates
[2]Department of Petroleum Geosciences, Khalifa University, Abu Dhabi, United Arab Emirates
[3]Department of Petroleum Engineering, Khalifa University, Abu Dhabi, United Arab Emirates
[4]Department of Mechanical Engineering, Khalifa University, Abu Dhabi, United Arab Emirates

Corresponding author: Mohamed Soufiane Jouini (mohamed.jouini@ku.ac.ae)

This work was supported in part by Abu Dhabi Department of Education and Knowledge (ADEK) in United Arab Emirates under Grant EX2018-024.

ABSTRACT Characterizing heterogeneity in reservoir rocks at the pore scale is crucial to understand the flow patterns better, and estimate reservoir petrophysical properties such as porosity and permeability. This study introduces multifractals as descriptors for rock samples' heterogeneity at the pore scale. We analyzed twenty rock samples from sandstone and carbonate reservoirs using their 3D X-ray micro-computed tomography images. In addition, we simulated porosity and permeability properties and examined their correlation with multifractal parameters. The results show that the capacity dimension D_0 and the information dimension D_1 correlate with porosity and permeability simulated from images, respectively. Finally, we calculated several multifractal parameters such as the width of the spectrum, the asymmetry degree of the spectrum in the horizontal direction and the value of the vertical difference between the two branches of the spectrum. Results illustrate the ability of multifractal parameters to classify groups of rock samples according to their degree of heterogeneity.

INDEX TERMS Heterogeneity, micro computed tomography, multifractals.

I. INTRODUCTION

Nowadays, image acquisition and analysis techniques provide powerful tools for characterizing the internal pore structure morphology of rock samples at high resolution, for example, using 3 D X-ray Micro-Computed Tomography (X-MCT), Nano-Computed Tomography, and 2D Scanning Electron Microscopy (SEM) images [1]–[3]. The general workflow consists of physically extracting a rock sample subset and scanning it at a resolution revealing pore space microstructure. Then, the pore network is extracted from digital images using image segmentation methods [4]. The resulting segmented binary images can be used to numerically simulate the porosity and permeability of the samples [3]–[4].

The associate editor coordinating the review of this manuscript and approving it for publication was Gerardo Di Martino.

Furthermore, using binary images, fractal and multifractals models can be implemented to quantify self-similarity parameters describing pore space microstructures [5]–[7]. Reference [7] introduced a flow equation by implementing fractal parameters estimated from the CT images of 10 limestones. Reference [8] used fractals to characterize geometrically pore structures of tight sandstone at multiple scales. Reference [9] introduced the concept of fractals to describe objects having scale power-law dependence. The fractal dimension model pattern changes according to the scale at which it is measured. In other words, the fractal dimension connects microscopic geometry patterns with macroscopic structures. Reference [10] used X-ray nano- and micro-computed tomography images of shale gas reservoirs to correlate fractal dimension to the experimental specific surface area, porosity and permeability. Reference [6] used X-MCT images of limestone

caprock for gas storage application and found that, after rock damage, permeability was positively correlated with the fractal dimension. Additionally, they noticed that some zones in analyzed rocks were not fractal, indicating decreased fractal dimension as confining pressure increased. In the literature, several studies showed that fractal models are suitable for homogeneous patterns but usually fail for irregular and complex data [11]–[14]. Such complexity may be encountered in many porous media, especially in carbonate reservoir rocks subject to deposition of sediments followed by diagenesis producing heterogeneous pore microstructures [4]–[5]. One of the first applications of multifractals for real systems was introduced by Mandelbrot to investigate energy dissipation on multiplicative cascades models [12]. In the literature, multifractal theory was used in several applications such as the modeling of benchmark Internet traffic in the telecommunication field [15]. In the medical field, multifractal theory was implemented in the diagnosing of diabetic retinopathy using Optical Coherence Tomography Angiography and also in the quantitative comparison of complexity between sequence of healthy and congestive heart failure groups [18]–[19]. In geosciences and petroleum engineering fields several studies implemented multifractals to study pore space distributions in reservoir rocks [5]–[7], [13]–[14], [16]–[17]. Measuring multifractals of the pore space phase mainly consists of measuring a statistical distribution to provide useful information about the pore structure heterogeneity. Reference [14] studied the multifractal spectrum of pore structures from segmented SEM images and used it to classify soil groups. Reference [16] correlated the multifractal spectrum estimated from pore structures in core samples with experimental air permeability measurements. Reference [5] studied the relationship between the multifractal spectrums of carbonate samples using SEM images acquired at different length scales. The study illustrated the relevance of using multifractal analysis to characterize the carbonate pore spaces heterogeneities quantitatively. Reference [20] implemented multifractal modeling to determine the T2 cutoffs of nuclear magnetic resonance spectroscopy of tight sandstone and coal. Reference [21] studied soil pore structures based on 3D X-MCT images. The authors implemented and compared box-counting and gliding cube methods to evaluate multifractal parameters in their study. Reference [22] described the existence of a relationship between multifractal parameters of Bakken shale with experimental measurements such as small-angle neutron scattering and mercury intrusion measurements. More recently, reference [17] illustrated the potential of using fractal dimensions for both 2D SEM and 3D X-MCT images to upscale porosity from the pore scale to the core plug scale.

Reference [9] discussed several techniques to calculate multifractal parameters, such as the box-counting and gliding box methods. A box-counting method is a classical approach; it is applied in several studies to estimate multifractal dimensions in porous media [5], [17], [21]. The method breaks down the spatial data extent into small cubical boxes analyzed at smaller scales. The procedure is equivalent to applying a magnification or a zoom to observe how image structures change with respect to the scale. The method can be applied to any 3D binary images to analyze the patterns with or without self-similarity.

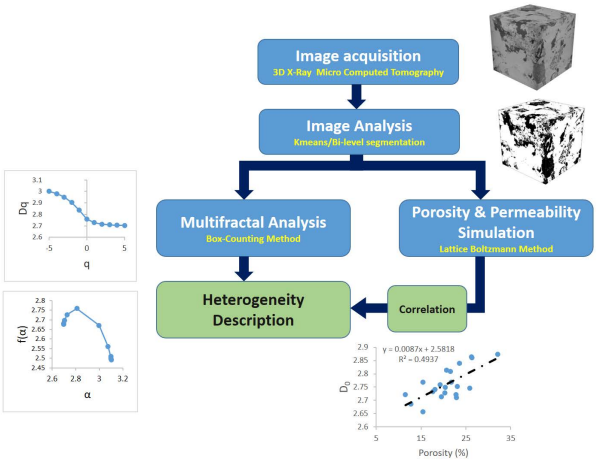

FIGURE 1. Multifractal and image analysis workflow to quantitatively study the heterogeneity of rock pore microstructures using 3D X-ray computed tomography images.

This study implemented multifractals modeling using the counting box method to characterize the heterogeneity of twenty-one samples from sandstones and carbonate reservoirs using 3D X-ray computed tomography images. Moreover, we numerically simulate the porosity and permeability values from 3D images. Furthermore, we study the correlation between multifractal parameters and simulated rock properties values. Finally, we identify the most relevant multifractal parameters allowing us to cluster image samples according to their heterogeneity. Figure 1 illustrates the general procedure implemented in this study.

II. MATERIALS AND METHODS

A. SAMPLES

This study implemented multifractal analysis in 3D X-ray micro-computed tomography images of twelve sandstone and nine carbonate samples extracted from reservoir zones. Eleven samples (S_1-S_{11}) represent different types of Berea sandstones publicly available through the Digital Rock Portal (https://www.digitalrocksportal.org/projects/317). The original sandstone samples consisted of 11 cylindrical core plugs with radii and heights of 19 mm and 38 mm, respectively [23]. Samples were acquired, first using X-ray microtomography at a coarse-scale then $8mm^3$ representative subset volumes were extracted and imaged for each sample. Each generated 3D X-ray computed tomography image represents a 1000^3 voxels data with a 2μm resolution. For example, the sample S_{12} is a $21mm^3$ subset extracted from a Fontainebleau sandstone and scanned at 7μm resolution. The carbonate samples (S_{13}-S_{20}) are physically available, extracted from oilfield reservoirs in the Middle East, and the sample S_{21} is Silurian dolomite [2], [5].

TABLE 1. List of rock samples and their respective experimental properties used in our study.

Type	Sample	Name	Resolution (μm)	Image size (mm^3)
Sandstone	S_1	BanderaGray	2	8
	S_2	Parker	2	8
	S_3	Kirby	2	8
	S_4	Bandera Brown	2	8
	S_5	Berea Sister Gray	2	8
	S_6	Brea Upper Gray	2	8
	S_7	Berea	2	8
	S_8	Castlegate	2	8
	S_9	Buff Berea	2	8
	S_{10}	Leopard	2	8
	S_{11}	Bentheimer	2	8
	S_{12}	Fontainbleau	7	343
Carbonate	S_{13}	*NA*	2	8
	S_{14}	*NA*	1	1
	S_{15}	*NA*	1	1
	S_{16}	*NA*	1	1
	S_{17}	*NA*	1	1
	S_{18}	*NA*	1	1
	S_{19}	*NA*	5	125
	S_{20}	*NA*	1	1
	S_{21}	Silurian Dolomite	5	125

The carbonate core plugs (S_{13}-S_{21}) are cylindrical samples with a 12.7 mm diameter and 25 mm height. Those samples were first scanned at a coarse scale of 13 μm resolution to detect the main heterogeneities. Subsequently, we extracted smaller subsets and scanned them at a finer scale, revealing a pore network [4]. Figure 2 illustrates some 2D slices extracted from the 1000^3 voxels 3D XMCT images for sandstones and carbonates. Table 1 summarizes the sample type, image acquisition resolutions, and sizes of the 21 samples.

In the following sections, we present the procedure illustrated in Figure 1. First, to calculate the multifractal parameters, we extracted the pore space from the generated 3D images. We used several image segmentation methods according to the grey level distribution complexity in the images. Then, we numerically simulated porosity and permeability properties using image analysis and Lattice Boltzmann methods. Furthermore, we calculated multifractal parameters and identified the most relevant ones allowing for clustering image samples according to their heterogeneity. Finally, we investigated potential relationships between multifractal parameters and the simulated rock properties.

B. IMAGE ANALYSIS

The literature review shows that two main approaches for 3D grey-level image segmentation can be reported, depending on data complexity [5], [24], [25]. Classical approaches are usually based on thresholding and spatial segmentation methods [26]–[27]. Thresholding algorithms are stochastic methods performing image segmentation by estimating grey levels separating image phases. These methods are suitable for data revealing multimodal histograms representing each phase. Otsu's algorithm and K-means are two examples of histogram shape-based methods [28]–[29]. Both techniques evaluate thresholds by minimizing the variance in each phase. Spatial approaches aim to include voxel spatial distribution information to segment image phases. An example of these approaches is the bi-level segmentation technique [30]. Classical methodologies are usually time-consuming and, in several cases, sensitive to noise. Recently new image segmentation approaches were developed thanks to the rapid advancement of deep learning techniques [31]–[32]. The first advantage of implementing such methods is the rapidity of the process. The second advantage is that these techniques do not need extra image processing, such as removing artifacts or filtering [33]. Nevertheless, the main limitation of this type of approach is that it requires a relatively large size of data for training purposes [32]. In this study, the twelve sandstone 3D images and the two carbonate samples S_{13} and S_{21} revealed bimodal distributions for the grey levels with a relatively small overlap, including between 5% and 15% of grey levels (see Figure 3). Thus, we applied a simple automatic Kmean's method to obtain the threshold value for each image. Due to the unresolved phase, the carbonate samples reveal a bimodal histogram with a relatively larger overlap between the two modes, including more than 15% of grey level values. For this reason, we applied the bi-level segmentation technique to obtain two thresholds and classify the image into solid matrix, pore space, and unresolved phases.

C. ROCK PROPERTIES SIMULATION

Rock properties were simulated using the pore space microstructure identified after applying the segmentation procedures [1], [4], [34]. For sandstone samples, the porosity was calculated as the ratio of the number of pore voxels to the total number of voxels in the image. For carbonate rocks, the porosity was estimated by including the proportion of voxels detected as pores. Then, we use the two thresholds to estimate the unresolved phase based on a linear interpolation between grey-level thresholds and porosities [4]. Using the Lattice Boltzmann Method (Lattice Boltzmann Method (LBM), permeability is simulated in sandstones and carbonates Indeed, the pore space microstructure represents a regular discrete grid used to define the LB lattice. This method models the fluid in terms of particles governed by an iterative time-dependent distribution following (1):

$$f(x + e_i, t + 1) = f(x, t) + \Omega(x, F, \tau, t, u_i) \quad (1)$$

In this equation, the independent variables x and t denote the particle location and the time, respectively. The particle streaming direction is denoted by e_i, where i stands for the index of a given direction in the lattice, u_i is the particle

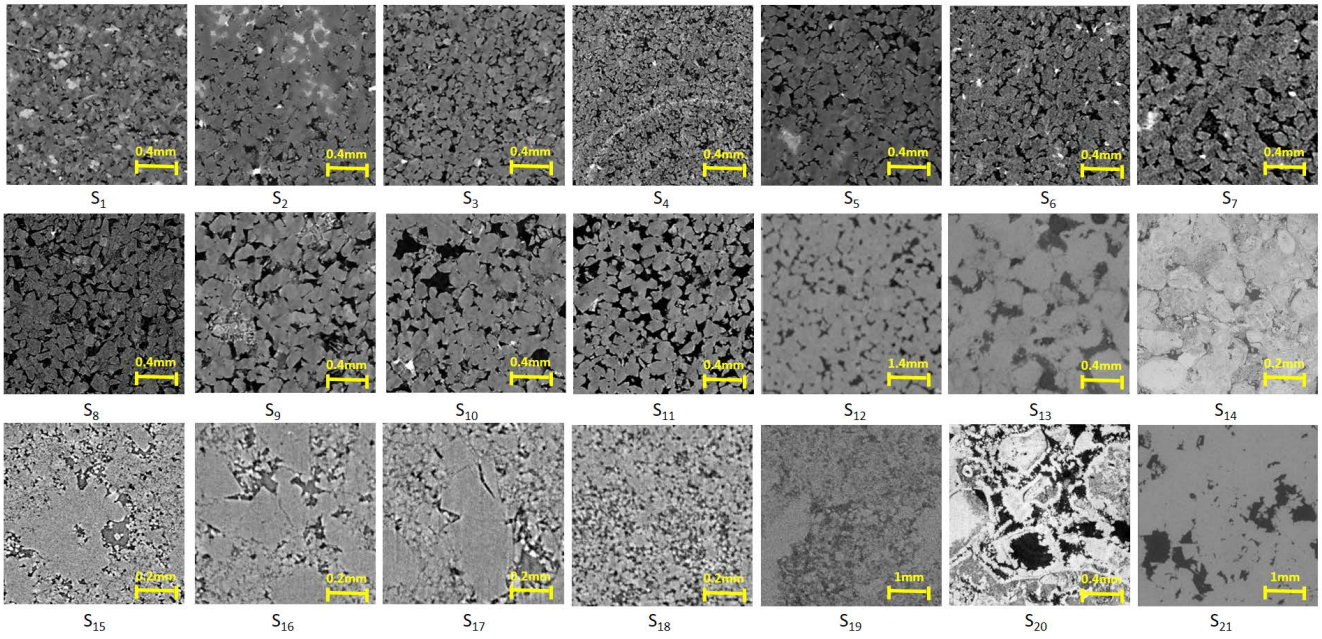

FIGURE 2. Original 2D sections images of 21 sandstone and carbonate rock samples (S_1 to S_{21}) extracted from their 3D X-ray computed tomography images.

velocity, Ω is a collision operator, τ is the relaxation time, and F is an external force term. Moreover, the Bhatnagar-Gross-Krook (LBGK) scheme for the 3D lattice was implemented [34]. A multi-relaxation-time model was used in the simulation with a D3Q19 as 3D model. We implemented the bounce-back rule to manage the solid-fluid internal boundaries. Furthermore, a no-slip-boundary condition was set at the solid-fluid interface. The flow was considered periodic between inlet and outlet. The procedure could be summarized into five main steps [35].

1) Compute the local density and momentum.
2) Calculate the post-collision state distribution of the particles.
3) Simulate the gradient of pressure as external force.
4) Move the distribution to neighboring nodes and compute the propagation step.
5) Repeat iteratively the four previous steps until reaching the steady state.

At the steady-state, the unidirectional Darcy's law calculates the permeability following (2).

$$K = \frac{\mu L Q}{A \Delta P}, \tag{2}$$

Here K represents the absolute permeability, Q stands for the flow, A is the surface section area, ΔP is the pressure difference along the length L of the sample, and μ is the dynamic fluid viscosity.

D. MULTIFRACTAL PARAMETERS

The main two advantages of implementing the box-counting method to estimate multifractal parameters are its simplicity and rapidity. Indeed, the box-counting method calculates the generalized multifractal dimensions using the proportion of the pore space detected in each cube of size ε. The generalized dimension D_q for the moment q evaluates the q^{th} order scaling properties of the data. For instance, in mono-fractal data, the number N of features of a given size ε varies following (3) and (4):

$$N(\varepsilon) \propto \varepsilon^{-D_0} \tag{3}$$

$$D_0 = \lim_{\varepsilon \to 0} \frac{logN(\varepsilon)}{log\frac{1}{\varepsilon}} \tag{4}$$

where D_0 is the fractal dimension for the moment q = 0.

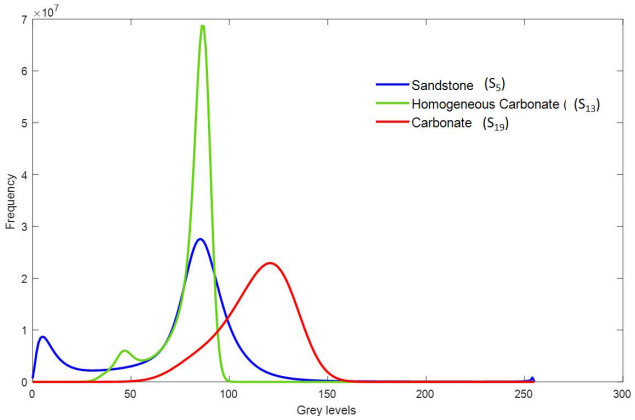

FIGURE 3. Examples of histograms calculated from 3D X-ray computed tomography images for a simple homogeneous sandstone (S_5), a homogeneous carbonate sample S_{13}, and a heterogeneous carbonate sample S_{19}.

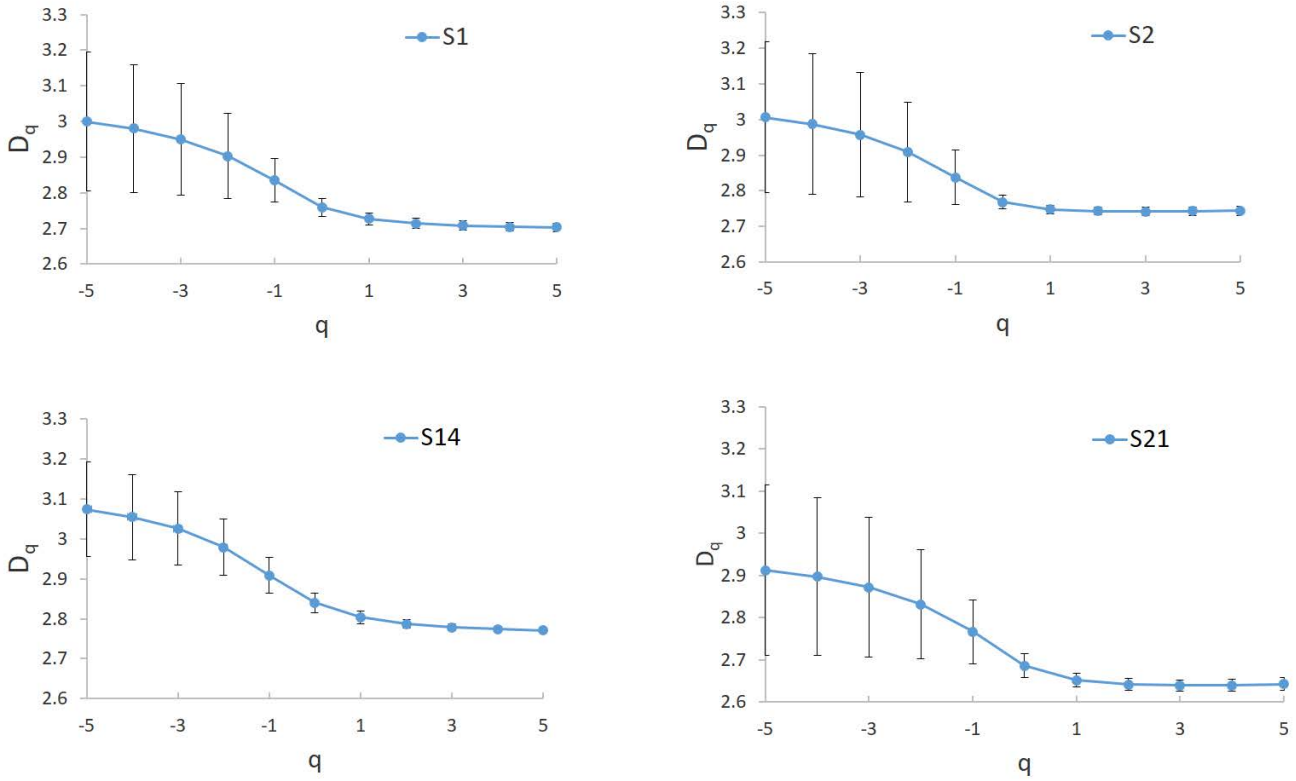

FIGURE 4. Examples of generalized multifractal dimensions calculated from 3D X-ray computed tomography images for two homogenous sandstones (S_1 and S_2), a heterogeneous carbonate sample S_{14}, and a homogeneous carbonate S_{21}.

For multifractal data, we define $P_j(\varepsilon)$ as the probability distribution in the j^{th} box. The generalized dimensions D_q and the partition function $X(q,\varepsilon)$ are defined for $q > 1$ in (5) and (6).

$$D_q = \frac{1}{q-1} \lim_{\varepsilon \to 0} \frac{log \sum_j P_j^q(\varepsilon)}{log\varepsilon} \tag{5}$$

$$X\,(q,\,\varepsilon) = \sum\nolimits_j P_j^q(\varepsilon) \tag{6}$$

For $q = 1$, D_1 is expressed as in (7):

$$D_1 = \lim_{\varepsilon \to 0} \frac{\sum_j P_j(\varepsilon) log P_j(\varepsilon)}{log\varepsilon} \tag{7}$$

The mass exponent τ_q is related to the generalized dimension D_1 through (8):

$$\tau_q = (q-1)D_q \tag{8}$$

Furthermore, the multifractal theory provides another important quantitative measure of the relationship between the Hausdorff dimension f and the average singularity α as in (9) and (10).

$$f\,(\alpha) = q\alpha - \tau_q \tag{9}$$

$$\alpha = \frac{d\,\tau_q}{dq} \tag{10}$$

Chhabra and Jensen [36] introduced a simple definition for the singularity spectrum based on (11) and (12).

$$f(q) = \lim_{\varepsilon \to 0} \frac{\sum_j \mu_j\,(q,\,\varepsilon) \log \mu_j\,(q,\,\varepsilon)}{log\varepsilon} \tag{11}$$

$$\alpha(q) = \lim_{\varepsilon \to 0} \frac{\sum_j \mu_j\,(q,\,\varepsilon) \log P_j\,(q,\,\varepsilon)}{log\varepsilon} \tag{12}$$

where $\mu_j\,(q,\,\varepsilon)$ illustrates the distortion of mass probability at a box compared to the distorted sum of all boxes at that size.

$$\mu_j\,(q,\,\varepsilon) = \frac{(P_j\,(\varepsilon))^q}{\sum_j (P_j\,(\varepsilon))^q} \tag{13}$$

The physical interpretation of the generalized dimensions D_q is reported in the literature for moments $q = \{0,\,1,\,2\}$. The generalized dimensions for these moments are called the capacity, the information, and the correlation dimensions respectively [37]. Reference [38] observed and proposed a relationship between the capacity dimension D_0 and the porosity of sandstone samples. Reference [14] used the information dimension D_1, which models the system entropy, to relate it to the permeability of sedimentary rocks. Reference [13] implemented the correlation dimension D_2 to evaluate the correlation of measures in boxes of different sizes.

The goal of the multifractal analysis is to study singularities in the images by using the singularity exponent α.

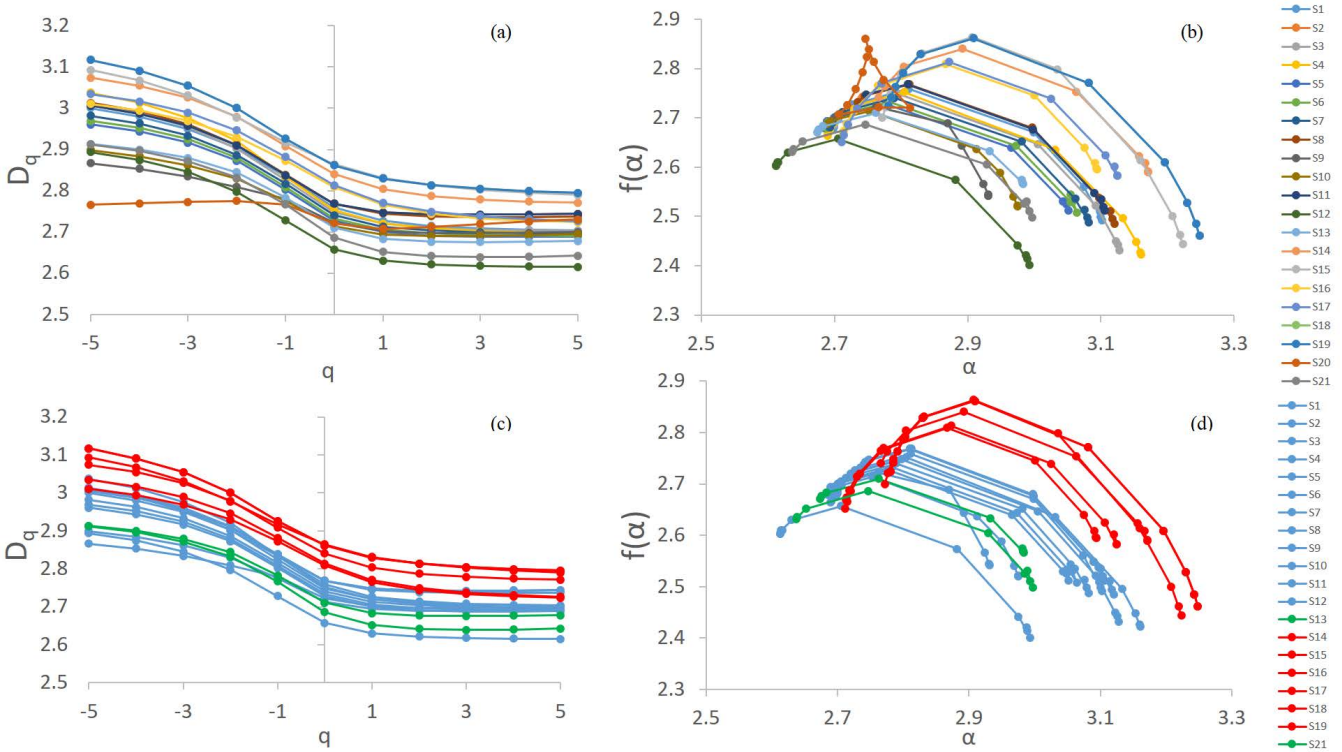

FIGURE 5. Multifractal parameters of pore microstructures from 3D X-ray micro-computed tomography images: (a) The generalized multifractal dimension D_q spectra for the twenty-one samples; (b) Singularity spectra for the twenty-one samples, (c) The generalized multifractal dimension D_q spectra according to the type of rocks; (d) Singularity spectra according to the type of rocks.

The width of the singularity spectrum $\Delta\alpha = [\alpha_{min}, \alpha_{max}]$ reflects the degree of heterogeneity of pore microstructures. The higher the complexity of pores structures is, the larger are $\Delta\alpha$ and the D_{qmax}-D_{qmin} distribution [39]–[40]. For homogeneous data $\Delta\alpha$ is small and the microstructure is considered monofractal when $\Delta\alpha = 0$. The singularity spectrum shape is a concave down parabola attaining its maximum at α_0. Furthermore, the parameters $H = (\alpha_0 - \alpha_{\max})$-$(\alpha_{\min} - \alpha_0)$ and $V = f(\alpha_{\min}) - f(\alpha_{\max})$ describe the asymmetry degree of the spectrum in the horizontal direction and the value of the vertical difference between the two branches of the spectrum, respectively.

III. RESULTS

A. MULTIFRACTAL PARAMETERS

To calculate the multifractal parameters using the box-counting method, we cropped the twenty images to extract 512^3 voxels blocks as the main input for Multifrac software which is an ImageJ plugin for multifractal analysis [41]. The generalized dimensions were calculated for the range $q_{min} = -5 < q < q_{max} = 5$. Figure 4 illustrates the generalized multifractal dimensions for two homogenous sandstones (S_1 and S_2), a heterogeneous carbonate sample S_{14} and a homogeneous carbonate S_{21}. The generalized multifractal dimension error shown in Figure 4 increases for negative moment values q, one of the main disadvantages of using the counting-box method as reported in previous studies [37]. Figure 5.a illustrates the generalized multifractal dimension D_q spectra of the twenty-one samples. D_q spectra follow a distinct decreasing reverse-shaped curve except for sample S_{20}. Figure 5.b reveals the singularity spectra calculated for the same samples. The general shape is a concave down parabola for all samples except sample S_{20}. The behavior of generalized dimension D_q curves and singularity spectra show that twenty data of the studied samples have multifractal characteristics.

Figure 5.c shows the generalized multifractal dimension D_q spectra according to the type of rocks. Sandstone samples are represented in blue color, and carbonate samples are represented in red color, while samples S_{13} and S_{21}, which are very homogeneous carbonate samples, are represented in green color. As expected, S_{13} and S_{21} reveal the same behavior as the sandstone samples due to their homogeneity. The same color classification was implemented for the singularity spectra representation in Figure 5.d. Whereas, Figure 5.c and Figure 5.d reveal that carbonate and sandstone groups have different ranges of variations in terms of multifractal moments and singularity spectra. Typically, the generalized spectral width of the sandstone samples group is lower than the carbonate samples group; this confirms the fact that sandstones are less heterogeneous that carbonates. Indeed, the average width of the singularity spectrum $\Delta\alpha$ for sandstone and carbonate samples are respectively 0.38 and

TABLE 2. Multifractal parameters for the rock samples.

Type	Sample	α_0	α_{min}	α_{max}	$\Delta\alpha$	$f(\alpha_{min})$	$f(\alpha_{max})$	V	D_{qmax}-D_{qmin}	H
Sandstone	S_1	2.79	2.69	3.09	.40	2.52	2.68	0.16	0.29	0.20
	S_2	2.77	2.73	3.10	0.37	2.51	2.73	0.22	0.29	0.29
	S_3	2.76	2.68	3.12	0.44	2.43	2.68	0.25	0.32	0.28
	S_4	2.79	2.65	3.16	0.51	2.42	2.65	0.23	0.31	0.23
	S_5	2.78	2.68	3.05	0.37	2.51	2.67	0.16	0.27	0.17
	S_6	2.78	2.69	3.06	0.37	2.50	2.68	0.18	0.27	0.19
	S_7	2.78	2.69	3.08	0.39	2.48	2.68	0.20	0.28	0.21
	S_8	2.79	2.72	3.12	0.40	2.48	2.71	0.23	0.27	0.26
	S_9	2.76	2.70	2.93	0.23	2.54	2.70	0.16	0.17	0.11
	S_{10}	2.75	2.69	2.97	0.28	2.52	2.69	0.17	0.2	0.16
	S_{11}	2.78	2.73	3.10	0.37	2.51	2.71	0.20	0.26	0.27
	S_{12}	2.70	2.61	2.99	0.38	2.41	2.60	0.19	0.28	0.20
Carbonate	S_{13}	2.76	2.67	2.98	0.31	2.56	2.67	0.11	0.24	0.13
	S_{14}	2.89	2.76	3.17	0.41	2.59	2.74	0.15	0.3	0.15
	S_{15}	2.90	2.77	3.22	0.45	2.44	2.70	0.26	0.3	0.19
	S_{16}	2.86	2.71	3.08	0.37	2.59	2.66	0.07	0.3	0.07
	S_{17}	2.87	2.71	3.12	0.41	2.58	2.65	0.07	0.31	0.09
	S_{18}	2.88	2.70	3.13	0.43	2.57	2.64	0.07	0.29	0.07
	S_{19}	2.90	2.78	3.24	0.46	2.46	2.72	0.26	0.32	0.22
	S_{21}	2.74	2.63	2.99	0.36	2.49	2.63	0.14	0.27	0.14

0.40 (see Table 2). If we exclude the two homogeneous carbonate samples from the carbonate group the average width of the singularity spectrum $\Delta\alpha$ for carbonate samples becomes 0.42. Furthermore, we calculated the average value of the asymmetry degree H for both sandstones and carbonates and found 0.21 and 0.13, respectively. The singularity spectra of sandstone samples reveal a higher asymmetry than carbonate samples but a narrower width. The average values of the vertical difference between the two branches of the spectrum H for sandstone and carbonate samples are 0.2 and 0.14, respectively. Furthermore, we calculated the average differences D_{qmax}-D_{qmin}(D_5-D_{-5}) for sandstone and carbonate samples and found 0.27 and 0.29, respectively.

Figure 6 shows the magnitude of α_0 at which the singularity spectrum parabola attains its maximum, calculated for each sample. We used color classification based on the type of study to illustrate the spatial distribution. Blue dots represent sandstone samples S_1-S_{12}, green dots represent the two homogeneous carbonate samples S_{13} and S_{21} and red dots represent the other carbonate samples. The plot shows two main clusters revealing the homogenous and heterogeneous groups of samples. The heterogeneous group has values of α_0 greater than 2.85, while the homogenous group reveals α_0 values less than 2.80.

Similarly, heterogeneous samples exhibit a width of singularity spectrum values $\Delta\alpha$ in the range [0.37, 0.46], whereas homogenous samples $\Delta\alpha$ lies within the interval [0.21, 0.51]. Additionally, the heterogeneity of pore microstructure can be related to the information dimension D_1. Indeed, the information dimension reflects the degree of concentration of the pores in the binary images. The larger the information D_1 is, the higher the pore microstructure heterogeneity [40]. The ranges of information dimension D_1 for the homogenous and heterogeneous groups are respectively [2.63, 2.74] and [2.70, 2.84] (Table 3).

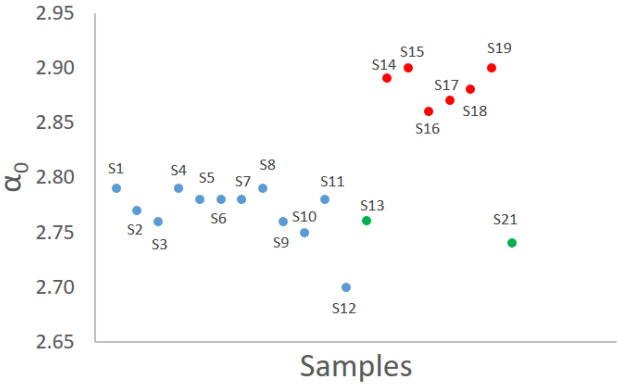

FIGURE 6. Multifractal parameter α_0. Blue dots represent sandstones samples S_1-S_{12}, green dots represent the two homogeneous carbonate samples S_{13} and S_{21} and red dots represent the other carbonate samples.

TABLE 3. Numerical simulation properties and first two moments.

Type	Sample	Porosity (%)	Permeability (mD)	D_0	D_1
Sandstone	S_1	19.2	15	2.7587	2.7267
	S_2	15.4	17	2.7682	2.7475
	S_3	20.4	84	2.7484	2.7203
	S_4	23.1	75	2.7522	2.7203
	S_5	20.3	70	2.7277	2.6997
	S_6	17.6	67	2.7327	2.7049
	S_7	18.1	111	2.7401	2.7122
	S_8	25.9	240	2.7450	2.7382
	S_9	22.8	243	2.7220	2.7014
	S_{10}	19.5	384	2.7136	2.6937
	S_{11}	21.7	351	2.7682	2.7475
	S_{12}	15.4	1240	2.6574	2.6301
Carbonate	S_{13}	22.9	141.8	2.7103	2.6827
	S_{14}	23.6	1.49	2.8403	2.8040
	S_{15}	26.2	5.35	2.8638	2.8313
	S_{16}	21.5	4.015	2.8093	2.7654
	S_{17}	20.7	5.1	2.8135	2.7701
	S_{18}	26.3	7.98	2.8613	2.8289
	S_{19}	32.1	17.3	2.8729	2.8440
	S_{20}	11.5	1490	2.7212	2.7070
	S_{21}	12.7	125.9	2.6863	2.6517

Besides, we investigated the ability of multifractal parameters to group samples according to their degree of heterogeneity. Figure 7.a shows the correlation between the three

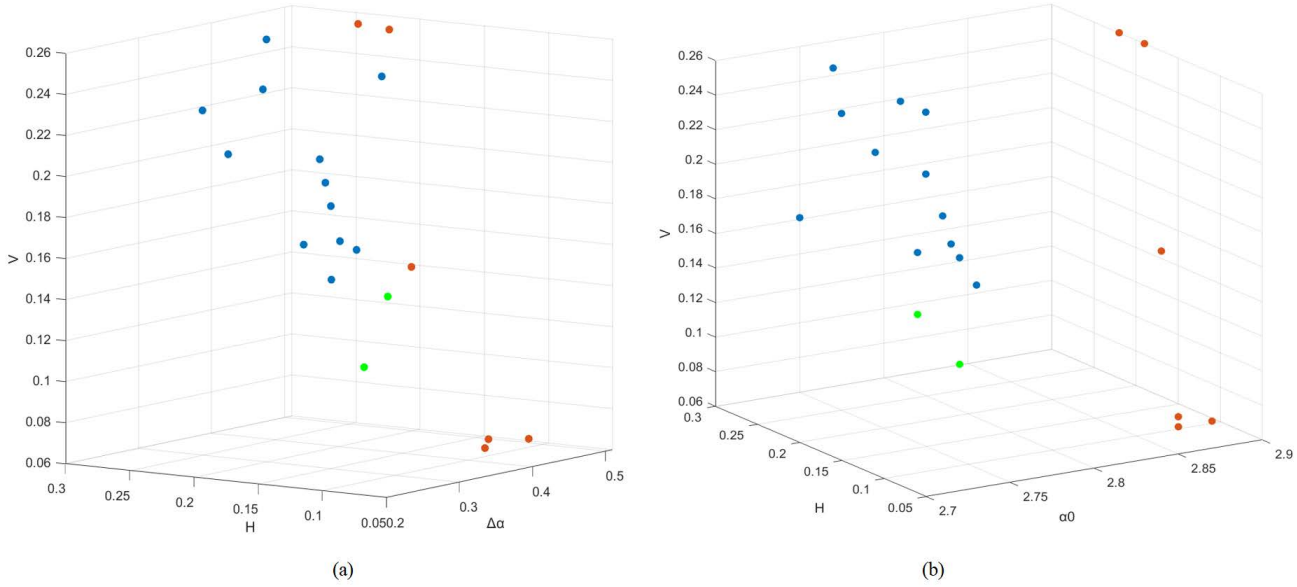

FIGURE 7. Multifractal parameters correlations: a) between $\Delta\alpha$, H and V, b) between α_0, H and V.

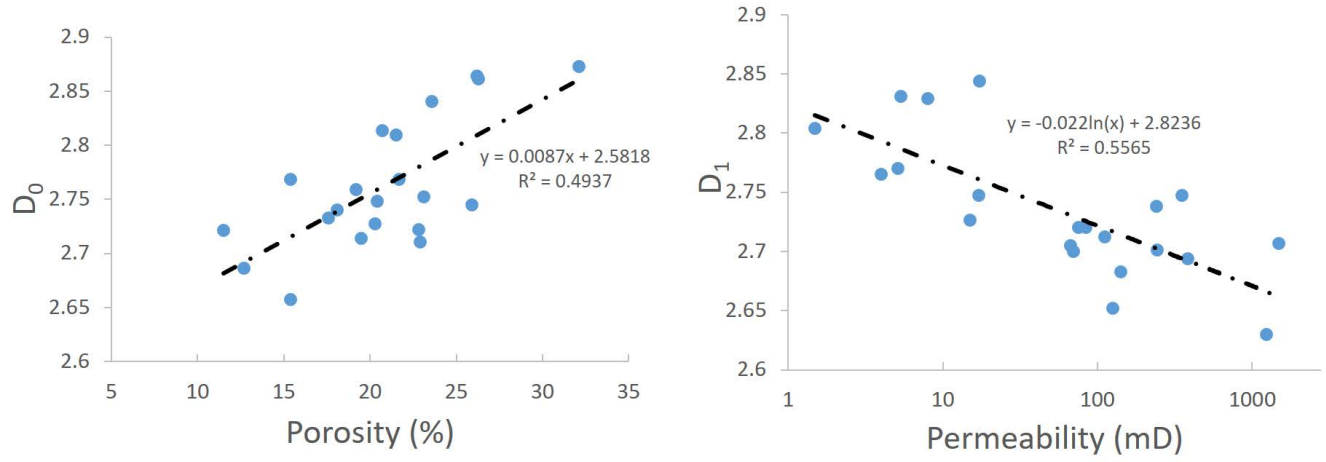

FIGURE 8. Multifractal and rock properties correlation: a) Cross plot between the porosity and the capacity dimension D_0, b) Cross plot between permeability and the information dimension D_1.

multifractal parameters $\Delta\alpha$, H, and V and reveals that dots corresponding to homogeneous and heterogeneous samples are laid out into two distinct areas, which are quite close spatially. The correlation between the multifractal parameters α_0, H, and V is depicted in Figure 7.b. The result shows a clear spatial separation between homogeneous and heterogeneous samples, indicating that α_0 is the most discriminating factor among the studied multifractal parameters.

B. MULTIFRACTAL AND ROCK PROPERTIES CORRELATION

To investigate the relationship between multifractal parameters and rock properties, we simulated the porosity and permeability of all available samples using their 3D segmented images (Table 3). Figure 8.a shows a positive correlation between the capacity dimension D_0 and the porosity with a correlation factor of 0.49. Figure 8.b reveals a negative correlation between permeability values and the information dimension D_1 with a correlation factor of 0.55. Both figures illustrate that capacity and information dimensions correlate with the porosity and the permeability, respectively, as reported in previous studies [37]–[38], [42]. Indeed, despite significant differences in pore microstructure between the carbonate and sandstone samples, we detect a relationship between D_0 and porosity, indicating that the total porosity is the main factor influencing the capacity dimension D_0. In addition, the relationships between the rock properties parameters and multifractal parameters were analyzed. Figure 9.a shows that α_0 linearly increases with the porosity for heterogeneous and homogeneous sample groups. The range of α_0 in each group clusters the samples accord-

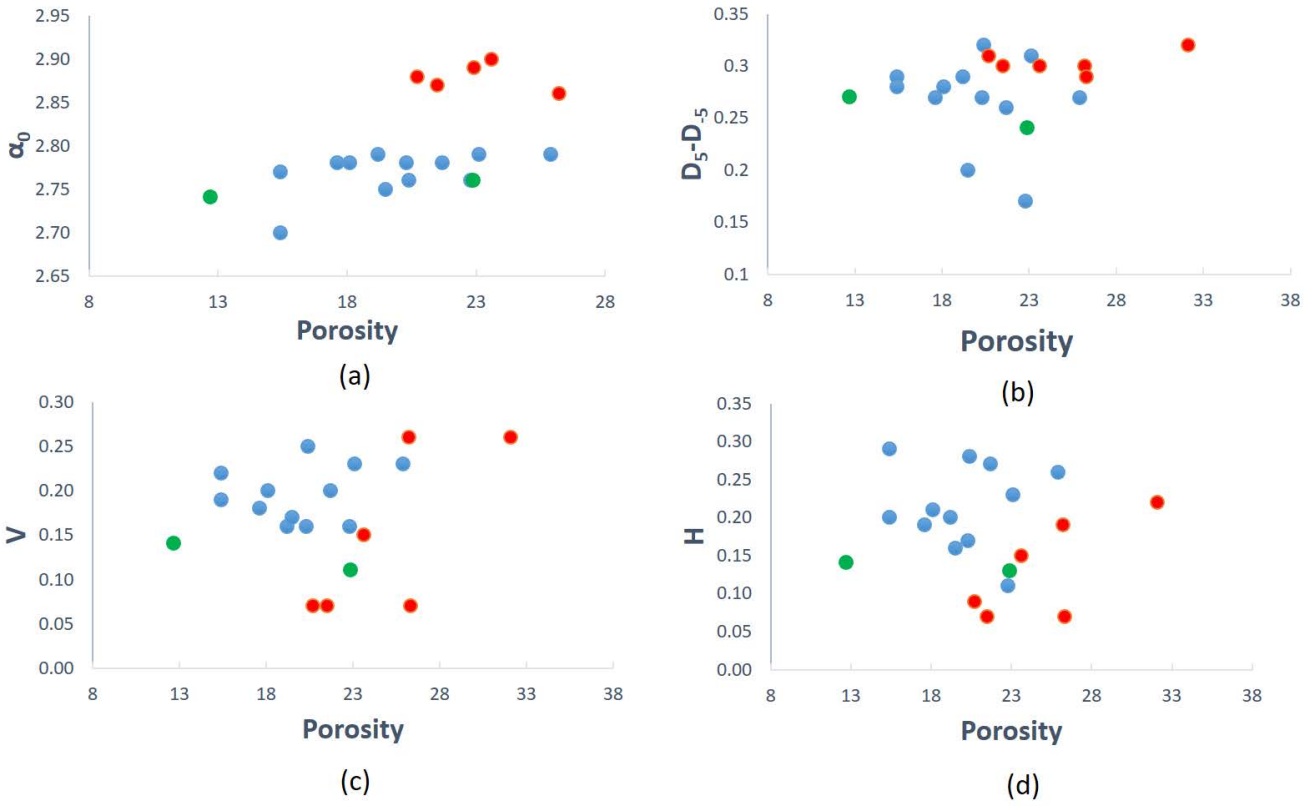

FIGURE 9. Multifractal and rock properties correlation: a) Cross plot between the porosity and α_0, b) Cross plot between porosity and the interval of generalized moments D_5-D_{-5}, c) Cross plot between the porosity and the vertical difference between the two branches of the spectrum $V = f(\alpha_{min})$-$f(\alpha_{max})$, d) Cross plot between porosity and $H = (\alpha_0 - \alpha_{max})$-$(\alpha_{min} - \alpha_0)$ describing the asymmetry of the singularity spectrum in the horizontal direction.

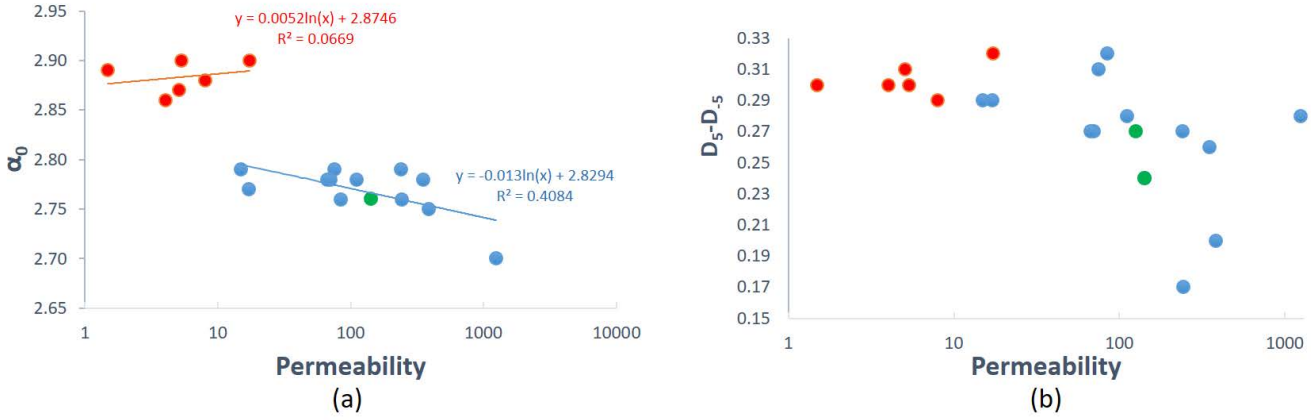

FIGURE 10. Multifractal and rock properties correlation: a) Cross plot between the permeability and α_0, b) Cross plot between permeability and the interval of generalized moments D_5-D_{-5}.

ing to their degrees of heterogeneity. Figure 9.b illustrates the relationship between porosity and the interval of generalized moments D_5-D_{-5}. As reported in the literature, larger D_5-D_{-5} values are associated with heterogeneous samples in general. However, several homogenous samples with D_5-D_{-5} are very close and larger than those associated with heterogeneous samples. Thus, this parameter alone cannot discriminate samples in two separated groups according to heterogeneity. Figure 9c reveals the relationship between the porosity and the value of the vertical difference between the two branches of the spectrum $V = f(\alpha_{max}) - f(\alpha_{min})$. Figure 8.c shows a larger variation when V values are associated with the heterogeneous samples compared to the homogeneous samples. Indeed, V values ranges in the interval [0.07,

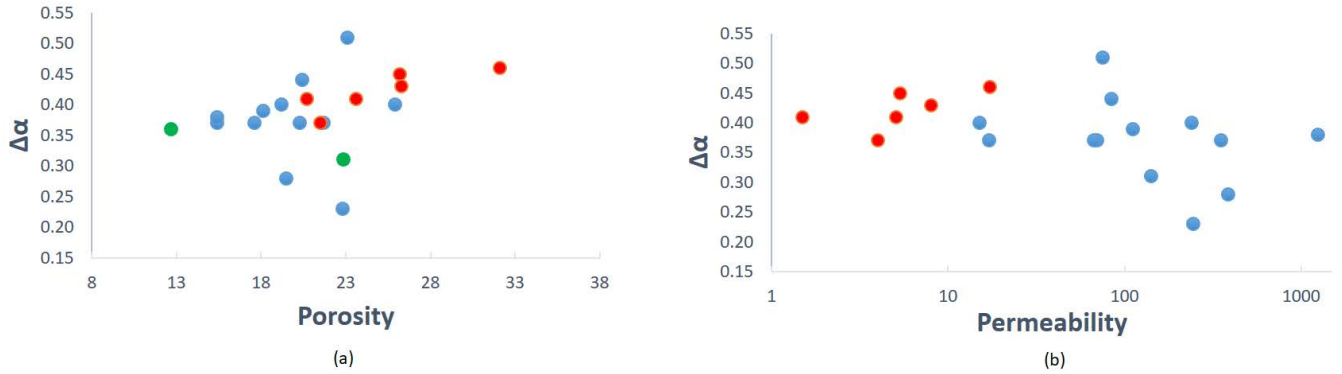

FIGURE 11. Rock properties correlation with width of singularity spectrum values $\Delta\alpha$: a) Cross plot between the porosity and $\Delta\alpha$, b) Cross plot between permeability and $\Delta\alpha$.

0.26] for heterogeneous samples and in the interval [0.16, 023] for homogeneous samples. Also, we observe that the scatter plot reveals two separate clusters of samples based on their heterogeneity. Figure 9.d shows the relationship between porosity and $H = (\alpha_0 - \alpha_{max}) - (\alpha_{min} - \alpha_0)$, describing the asymmetry of the singularity spectrum in the horizontal direction. The ranges of variation for H values for homogeneous and heterogeneous samples are respectively [0.11, 0.29] and [0.07, 0.22].

Figure 10 illustrates the relationships between the permeability and multifractal parameters α_0 and D_5-D_{-5}. This figure confirms previous observations obtained for porosity. Figure 10.a shows that α_0 linearly decreases with the permeability for heterogeneous samples only. However, the correlation coefficient calculated for homogeneous samples does not reveal any linear relationship between $\alpha_0$and the permeability. Figures 11.a and 11.b reveal the relationship between the width of singularity spectrum values $\Delta\alpha$ and rock samples' simulated porosity and permeability. Both plots show that $\Delta\alpha$ is a relevant parameter for clustering samples based on their heterogeneity.

IV. CONCLUSION

This paper investigated the use of multifractal parameters to quantitatively evaluate the heterogeneity of the pore microstructure of twenty-one sandstones and digital carbonate rocks. The conclusions are as follows:

(1) The behavior of generalized dimension D_q curves and singularity spectra show that twenty samples among the twenty-one analyzed have multifractal characteristics.

(2) The capacity dimension D_0 and the information dimension D_1 correlate with the simulated porosity and permeability values. Indeed, a direct linear relationship exists between the simulated porosity and D_0, whereas an indirect linear relationship exists between the logarithm of permeability values and D_1.

(3) Only the multifractal parameters α_0 and $\Delta\alpha$ show different ranges of variation according to the heterogeneity of the rock samples. The parameters $H = (\alpha_0 - \alpha_{max}) - (\alpha_{min} - \alpha_0)$, and $V = f(\alpha_{min}) - f(\alpha_{max})$ show overlaps in their values for homogeneous and heterogeneous rock samples which indicates that they not suitable for discriminating the groups of samples according to their heterogeneity.

ACKNOWLEDGMENT

The authors would like to thank Halliburton Ingrain Abu Dhabi for their collaboration and fruitful discussions and collaboration for data acquisition.

REFERENCES

[1] M. S. Jouini and S. D. Vega, "Simulation of elastic properties in carbonates," *Lead. Edge*, vol. 30, no. 12, pp. 1400–1407, 2011, doi: 10.1190/1.3672485.

[2] T. F. Faisal, A. Islam, M. S. Jouini, R. S. Devarapalli, M. Jouiad, and M. Sassi, "Numerical prediction of carbonate elastic properties based on multi-scale imaging," *Geomech. Energy Environ.*, vol. 20, pp. 100–125, Dec. 2019, doi: 10.1016/j.gete.2019.100125.

[3] M. S. Jouini, A. AlSumaiti, M. Tembely, F. Hjouj, and K. Rahimov, "Permeability upscaling in complex carbonate samples using textures of micro-computed tomography images," *Int. J. Model. Simul.*, vol. 40, no. 4, pp. 245–259, 2020, doi: 10.1080/02286203.2019.1596728.

[4] M. S. Jouini, S. Vega, and A. Al-Ratrout, "Numerical estimation of carbonate rock properties using multiscale images," *Geophys. Prospecting*, vol. 63, no. 2, pp. 405–421, Mar. 2015, doi: 10.1016/j.apm.2016.09.021.

[5] M. S. Jouini, S. Vega, and E. A. Mokhtar, "Multiscale characterization of pore spaces using multifractals analysis of scanning electronic microscopy images of carbonates," *Nonlinear Processes Geophys.*, vol. 18, no. 6, pp. 941–953, 2011, doi: 10.5194/npg-18-941-2011.

[6] A. Zhu, J. Liu, G. Ding, Z. Wu, X. Shi, and Y. Zeng, "Experimental investigation on permeability, mesodamage and fractal characteristics of limestone caprock under THM coupling based on μCT technology," *J. Petroleum Sci. Eng.*, vol. 212, pp. 110–197, May 2022, doi: 10.1016/j.petrol.2022.110197.

[7] F. Wang, L. Jiao, P. Lian, and J. Zeng, "Apparent gas permeability, intrinsic permeability and liquid permeability of fractal porous media: Carbonate rock study with experiments and mathematical modelling," *J. Petroleum Sci. Eng.*, vol. 173, pp. 1304–1315, Feb. 2019, doi: 10.1016/j.petrol.2018.10.095.

[8] W. Lin, Z. Wu, X. Li, Z. Yang, M. Hu, D. Han, C. Wang, and J. Zhang, "Digital characterization and fractal quantification of the pore structures of tight sandstone at multiple scales," *J. Petroleum Explor. Prod. Technol.*, pp. 1–11, May 2022, doi: 10.1007/s13202-022-01502-4.

[9] B. B. Mandelbrot, *The Fractal Geometry of Nature*. New York, NY, USA: Freeman, 1977.

[10] M. S. Rahner, M. Halisch, C. P. Fernandes, A. Weller, and V. S. S. Dos Santos, "Fractal dimensions of pore spaces in unconventional reservoir rocks using X-ray nano- and micro-computed tomography," *J. Natural Gas Sci. Eng.*, vol. 55, pp. 298–311, Jul. 2018, doi: 10.1016/j.jngse.2018.05.011.

[11] T. B. Zeleke and B. C. Si, "Characterizing scale-dependent spatial relationships between soil properties using multifractal techniques," *Geoderma*, vol. 134, nos. 3–4, pp. 440–452, Oct. 2006, doi: 10.1016/j.geoderma.2006.03.013.
[12] B. B. Mandelbrot, "Intermittent turbulence in self-similar cascades: Divergence of high moments and dimension of the carrier," *J. Fluid Mech.*, vol. 62, no. 2, pp. 331–358, Jan. 1974, doi: 10.1017/S0022112074000711.
[13] A. Posadas, D. Gimenez, R. Quiroz, and R. Protz, "Multifractal characterization of soil pore systems," *Soil Sci. Soc. Amer. J.*, vol. 67, no. 5, pp. 1361–1369, 2003, doi: 10.2136/sssaj2003.1361.
[14] J. M'uller and J. L. McCauley, "Implication of fractal geometry for fluid flow properties of sedimentary rocks," *Transp. Porous Media*, vol. 8, pp. 133–147, Jun. 1992, doi: 10.1007/BF00617114.
[15] Y. Yu, M. Song, Y. Fu, and J. Song, "Traffic prediction in 3G mobile networks based on multifractal exploration," *Tsinghua Sci. Technol.*, vol. 18, no. 4, pp. 398–405, Aug. 2013, doi: 10.1109/TST.2013.6574678.
[16] J. Müller, "Characterization of pore space in chalk by multifractal analysis," *J. Hydrol.*, vol. 187, nos. 1–2, pp. 215–222, 1996, doi: 10.1016/S0022-1694(96)03097-1.
[17] M. J. Munawar, S. Vega, C. Lin, M. Alsuwaidi, N. Ahsan, and R. R. Bhakta, "Upscaling reservoir rock porosity by fractal dimension using three-dimensional micro-computed tomography and two-dimensional scanning electron microscope images," *J. Energy Resour. Technol.*, vol. 143, no. 1, pp. 003–013, Jan. 2021, doi: 10.1115/1.4047589.
[18] S. Li, "Multifractal detrended fluctuation analysis of congestive heart failure disease based on constructed heartbeat sequence," *IEEE Access*, vol. 8, pp. 205244–205249, 2020, doi: 10.1109/ACCESS.2020.3037080.
[19] M. M. Abdelsalam and M. A. Zahran, "A novel approach of diabetic retinopathy early detection based on multifractal geometry analysis for OCTA macular images using support vector machine," *IEEE Access*, vol. 9, pp. 22844–22858, 2021, doi: 10.1109/ACCESS.2021.3054743.
[20] P. Zhao, Z. Wang, Z. Sun, J. Cai, and L. Wang, "Investigation on the pore structure and multifractal characteristics of tight oil reservoirs using NMR measurements: Permian Lucaogou formation in Jimusaer Sag, Junggar Basin," *Marine Petroleum Geol.*, vol. 86, pp. 1067–1081, Sep. 2017, doi: 10.1016/j.marpetgeo.2017.07.011.
[21] I. G. Torre, J. C. Losada, R. J. Heck, and A. M. Tarquis, "Multifractal analysis of 3D images of tillage soil," *Geoderma*, vol. 311, pp. 167–174, Feb. 2018, doi: 10.1016/j.geoderma.2017.02.013.
[22] K. Liu, M. Ostadhassan, and L. Kong, "Fractal and multifractal characteristics of pore throats in the Bakken Shale," *Transp. Porous Media*, vol. 126, no. 3, pp. 579–598, 2019, doi: 10.1007/s11242-018-1130-2.
[23] R. F. Neumann, M. Barsi-Andreeta, E. Lucas-Oliveira, H. Barbalho, W. A. Trevizan, T. J. Bonagamba, and M. B. Steiner, "High accuracy capillary network representation in digital rock reveals permeability scaling functions," *Sci. Rep.*, vol. 11, no. 1, p. 11370, Dec. 2021, doi: 10.1038/s41598-021-90090-0.
[24] F. Meyer and S. Beucher, "Morphological segmentation," *J. Vis. Commun. Image Represent.*, vol. 1, no. 1, pp. 21–46, 1990.
[25] W.-H. Chao, Y.-Y. Chen, S.-H. Lin, Y.-Y.-I. Shih, and S. Tsang, "Automatic segmentation of magnetic resonance images using a decision tree with spatial information," *Computerized Med. Imag. Graph.*, vol. 33, no. 2, pp. 111–121, Mar. 2009.
[26] L. Vincent and P. Soille, "Watersheds in digital spaces: An efficient algorithm based on immersion simulations," *Pattern Anal. Mach. Intell.*, vol. 13, no. 6, pp. 583–598, 1991.
[27] H. J. Vogel and A. Kretzschmar, "Topological characterization of pore space in soil—Sample preparation and digital image processing," *Geoderma*, vol. 73, pp. 29–38, Sep. 1996.
[28] N. Otsu, "A threshold selection method from gray-level histograms," *IEEE Trans. Syst., Man, Cybern.*, vol. SMC-9, no. 1, pp. 62–66, Jan. 1979.
[29] J. B. MacQueen, "Some methods for classification and analysis of multivariate observations," in *Proc. Berkeley Symp. Math. Statist. Probab.* Berkeley, CA, USA: Univ. California Press, 1967, pp. 281–297.
[30] S. Schluter, U. Weller, and H. J. Vogel, "Segmentation of X-ray microtomography images of soil using gradient masks," *Comput. Geosci.*, vol. 36, no. 10, pp. 1246–1251, 2010.
[31] Y. LeCun, Y. Bengio, and G. Hinton, "Deep learning," *Nature*, vol. 521, no. 7553, p. 436, May 2015.
[32] Y. Li, M. Lingfei, Z. Zhong, F. Liu, M. A. Chapman, D. Cao, and J. Li, "Deep learning for LiDAR point clouds in autonomous driving: A review," *IEEE Trans. Neural Netw. Learn. Syst.*, vol. 32, no. 8, pp. 3412–3432, Aug. 2020, doi: 10.1109/TNNLS.2020.3015992.
[33] J. Phan, L. C. Ruspini, and F. Lindseth, "Automatic segmentation tool for 3D digital rocks by deep learning," *Sci. Rep.*, vol. 11, no. 1, p. 19123, Dec. 2021, doi: 10.1038/s41598-021-98697-z.
[34] M. Tembely, A. AlSumaiti, M. Jouini, and K. Rahimov, "The effect of heat transfer and polymer concentration on non-newtonian fluid from pore-scale simulation of rock X-ray micro-CT," *Polymers*, vol. 9, no. 12, p. 509, Oct. 2017, doi: 10.3390/polym9100509.
[35] R. S. Maier, R. S. Bernard, and D. W. Grunau, "Boundary conditions for the lattice Boltzmann method," *Phys. Fluids*, vol. 8, no. 7, pp. 1788–1801, 1996.
[36] W. Lin, S. Xiong, Y. Liu, Y. He, S. Chu, and S. Liu, "Spontaneous imbibition in tight porous media with different wettability: Pore-scale simulation," *Phys. Fluids*, vol. 33, no. 3, Mar. 2021, Art. no. 032013, doi: 10.1063/5.0042606.
[37] A. Chhabra and R. V. Jensen, "Direct determination of the f(α) singularity spectrum," *Phys. Rev. Lett.*, vol. 62, pp. 1327–1330, Mar. 1989.
[38] H. G. E. Hentschel and I. Procaccia, "The infinite number of generalized dimensions of fractals and strange attractors," *Phys. D, Nonlinear Phenomena*, vol. 8, no. 3, pp. 435–444, Sep. 1983.
[39] M. Guan, X. Liu, Z. Jin, and J. Lai, "The heterogeneity of pore structure in lacustrine shales: Insights from multifractal analysis using N_2 adsorption and mercury intrusion," *Mar. Petroleum Geol.*, vol. 114, pp. 104–150, Apr. 2020.
[40] F. San José Martínez, M. A. Martín, F. J. Caniego, M. Tuller, A. Guber, Y. Pachepsky, and C. García-Gutiérrez, "Multifractal analysis of discretized X-ray CT images for the characterization of soil macropore structures," *Geoderma*, vol. 156, nos. 1–2, pp. 32–42, Apr. 2010, doi: 10.1016/j.geoderma.2010.01.004.
[41] P. Su, Z. Xia, P. Wang, W. Ding, Y. Hu, W. Zhang, and Y. Peng, "Fractal and multifractal analysis of pore size distribution in low permeability reservoirs based on mercury intrusion porosimetry," *Energies*, vol. 12, no. 7, p. 1337, Apr. 2019, doi: 10.3390/en12071337.
[42] I. G. Torre, R. J. Heck, and A. M. Tarquis, "MULTIFRAC: An ImageJ plugin for multiscale characterization of 2D and 3D stack images," *SoftwareX*, vol. 12, Jul. 2020, Art. no. 100574, doi: 10.1016/j.softx.2020.100574.
[43] A. J. Katz and A. H. Thompson, "Fractal sandstone pores: Implications for conductivity and Pore formation," *Phys. Rev. Lett.*, vol. 54, pp. 1325–1328, Mar. 1985, doi: 10.1103/PhysRevLett.54.1325.

MOHAMED SOUFIANE JOUINI received the M.E. degree in electrical engineering from the École Nationale Supérieure d'Électrotechnique, d'Électronique, d'Informatique, d'Hydraulique et des Télécommunications, Toulouse, France, in 2004, the M.S. degree in signal and image processing from the National Polytechnic Institute of Toulouse, France, in 2005, and the Ph.D. degree in signal and image processing from the University of Bordeaux, France, in 2009. From 2009 to 2010, he was a Research Scientist with SAGEM MORPHO Paris, France. Then, he was a Research Scientist with the Petroleum Institute Abu Dhabi, United Arab Emirates. In 2014, he was promoted as an Assistant Professor, and then, as an Associate Professor with the Mathematics Department, Khalifa University, Abu Dhabi, in 2020.

FATEH BOUCHAALA received the Ph.D. degree in marine geoscience from the Marine European Institute, France. His research interest includes the study of wave propagation from micro (Mega-Hertz) to macro scale (less than one Hertz). His research has direct applications on study of earthquakes, petroleum exploration, and construction engineering. He is an active member of several geophysical and engineering associations. He is also an Active Reviewer for several international peer reviewed journals namely, *Geophysics*, *Geophysical Prospecting*, *Geophysical Journal International*. He is an Associate Editor of *Petroleum & Petrochemical Engineering Journal*.

MOHAMED KAMEL RIAHI received the Ph.D. degree in applied mathematics from Pierre et Marie Curie University, Paris, France.

He has worked as a Postdoctoral Research Associate with the Department of Mathematical Sciences, New Jersey Institute of Technology, USA, and the DeFI Team, INRIA-Saclay Palaiseau France, as a Postdoctoral Researcher. He is currently an Expert in scientific computing and numerical analysis related to partial differential equations. His research interests include and is not limited to space- time-domain decomposition methods, finite element method, integral equations method, numerical optimization, iterative method, preconditioning technique, shape optimization, optimal control problem, high-performance computing, and parallel programming. He applies his research on waves related problems (acoustics and electromagnetism), fluid-structure interaction, heat and mass transfer, and inverse problems. He is serving as referee for several peer-reviewed applied mathematical journals.

MOHAMED SASSI is currently a Highly Qualified Professor of mechanical/chemical engineering with over 30 years of multi-disciplinary progressive experience in academia and industry with very good expertise in academic program development, management, and assessment. In research, he is also an Internationally Known Expert in thermo-fluids, combustion, air pollution control, carbon capture and sequestration, optical and spectroscopic diagnostics and analysis methods, computational fluid dynamics (CFD) with chemical kinetics simulation, and technology development for clean energy and environmental protection applications in general. Lately, he has been very much involved and funded for Digital Rock Physics (DRP), Enhanced Oil Recovery (EOR), and multiphase flow in porous media. He has a worldwide work experience and strength in the USA, Europe, and Middle East North Africa (MENA) region.

HAMID ABDERRAHMANE received the Ph.D. degree from Concordia University, Montreal, Canada, in 2009. Prior to joining Khalifa University, he was a Postdoctoral Fellow with McGill University, Canada, and a Postdoctoral Fellow with the King Abdullah University of Science and Technology (KAUST), Saudi Arabia. He has published 41 research papers in top-notch journals, including *Physical Review Letters*, *Journal of Fluid Mechanics*, *Physics of Fluids*, *Physical Review E*, and 45 papers in international conference proceedings. His research interests include the areas of the general fields of fluid mechanics and fluid-structure interactions with a particular focus on nonlinear dynamics in fluid-structure interactions and hydrodynamic instabilities. Apart from his research involvement, he served for many years as a Teaching Assistant and a Lecturer of various courses at the university level. He was awarded the two prestigious Postdoctoral Scholarships in Canada and Quebec. His Ph.D. work was honored as one of the top ten discoveries by Quebec Science Magazine, in 2009. His work on flow visualizations received the prestigious Milton Van Dyke Award, Gallery of Fluid Motion, in 2010.

FAWAZ HJOUJ received the B.A. and M.Sc. degrees in mathematics and the Ph.D. degree in mathematics from Southern Illinois University, USA. He has also taken graduate courses in statistics. From 2004 to 2013, he worked as an Assistant Professor with the Mathematics Department, East Carolina University, USA, where he taught mathematics to engineering students and statistics. In 2013, he joined the Petroleum Institute, United Arab Emirates, which became a part of the Khalifa University of Science and Technology, in 2017. His research interests include radon transformation that synthesizes numerical analysis and Fourier analysis. This includes computations on digital image processing with applications to the field of computerized tomography. Within this framework, he conducts activities at two levels—the first level is original research and includes the development of new ideas. The second level introduces certain subjects from this field to undergraduate instruction and research. He has created and published simplified introductions for undergraduate students in a range of subjects, including mathematics and engineering sciences, among others. For example, it is well known that viewing a section of the body without interference from other regions have long been a goal of radiologists and engineers, and that these goals have been achieved through CT, MRI, PET, and other forms of tomography. The modules that, he has developed on tomography help readers appreciate this technology and the underlying mathematics.